LETTER

https://doi.org/10.1038/s41586-019-1358-1

Magnetic monopole noise

Ritika Dusad[1,10], Franziska K. K. Kirschner[2,10], Jesse C. Hoke[1,3], Benjamin R. Roberts[1], Anna Eyal[1,4], Felix Flicker[5], Graeme M. Luke[6,7,8], Stephen J. Blundell[2]* & J. C. Séamus Davis[1,2,9]*

Magnetic monopoles[1–3] are hypothetical elementary particles with quantized magnetic charge. In principle, a magnetic monopole can be detected by the quantized jump in magnetic flux that it generates upon passage through a superconducting quantum interference device (SQUID)[4]. Following the theoretical prediction that emergent magnetic monopoles should exist in several lanthanide pyrochlore magnetic insulators[5,6], including $Dy_2Ti_2O_7$, the SQUID technique has been proposed for their direct detection[6]. However, this approach has been hindered by the high number density and the generation–recombination fluctuations expected of such thermally generated monopoles. Recently, theoretical advances have enabled the prediction of the spectral density of magnetic-flux noise from monopole generation–recombination fluctuations in these materials[7,8]. Here we report the development of a SQUID-based flux noise spectrometer and measurements of the frequency and temperature dependence of magnetic-flux noise generated by $Dy_2Ti_2O_7$ crystals. We detect almost all of the features of magnetic-flux noise predicted for magnetic monopole plasmas[7,8], including the existence of intense magnetization noise and its characteristic frequency and temperature dependence. Moreover, comparisons of simulated and measured correlation functions of the magnetic-flux noise indicate that the motions of magnetic charges are strongly correlated. Intriguingly, because the generation–recombination time constant for $Dy_2Ti_2O_7$ is in the millisecond range, magnetic monopole flux noise amplified by SQUID is audible to humans.

Observation of a quantized jump in the magnetic flux Φ threading a SQUID loop is the definitive technique for the detection of magnetic monopoles[4] (Fig. 1a). For example, an elementary Dirac monopole[1] with magnetic charge $m_0 = \pm h/(\mu_0 e)$ (h is Planck's constant; e is the electron charge; μ_0 is the magnetic constant) should generate a flux change of $\Phi_0 = \pm h/e$ upon passage through a SQUID loop. This approach was proposed[6] for the detection of thermally generated magnetic monopoles, each with magnetic charge $\pm m_*$, in lanthanide pyrochlore magnetic insulators[9,10] such as $Dy_2Ti_2O_7$ and $Ho_2Ti_2O_7$. If each monopole in a thermally generated $\pm m_*$ pair departs to $\pm\infty$ in opposite directions, the net flux threading the SQUID loop should evolve from 0 to $\Phi_* = m_*\mu_0$ (Fig. 1b). However, because these materials are hypothesized to contain a dense monopole plasma, with equal numbers of $\pm m_*$ magnetic charges undergoing rapid thermal generation and recombination (GR), the $\Phi(t)$ measured by a SQUID (Fig. 1c) should be stochastic and weak. Thus, despite extensive evidence consistent with a magnetic monopole plasma[9,10] in $Dy_2Ti_2O_7$ and $Ho_2Ti_2O_7$, the magnetic-flux signature[4,6] of the magnetic charges m_* has gone undetected.

In these compounds, the magnetic ions (Dy^{3+}, Ho^{3+}) occupy vertices of corner-sharing tetrahedra (Fig. 1d). Each ion exhibits only two spin configurations and acts as an Ising magnetic moment ($\mu \approx 10\mu_B$; μ_B, Bohr magneton) that points either towards ('in') or away from ('out') the centre of each tetrahedron[9,11] (black arrows in Fig. 1d). The nearest-neighbour exchange interaction between these moments[9] takes the form $-J\sum \mathbf{S}_i\cdot\mathbf{S}_j$, with exchange energy $J \approx -3.7$ K for $Dy_2Ti_2O_7$ and $J \approx -1.6$ K for $Ho_2Ti_2O_7$ and $\mathbf{S}_i$ the unit vector representing an Ising moment on site i. The resulting dipolar spin ice (DSI) Hamiltonian incorporates both the exchange interactions and longer-range dipole interactions as[12]

$$H = -J\sum_{i,j} \mathbf{S}_i\cdot\mathbf{S}_j + Da^3\sum_{i<j}\left[\frac{\mathbf{S}_i\cdot\mathbf{S}_j}{|\mathbf{r}_{ij}|^3} - \frac{3(\mathbf{S}_i\cdot\mathbf{r}_{ij})(\mathbf{S}_j\cdot\mathbf{r}_{ij})}{|\mathbf{r}_{ij}|^5}\right] \tag{1}$$

Here $D = \mu_0\mu^2/(4\pi a^3)$ is the dipole-interaction energy scale ($D = +1.41$ K for both $Dy_2Ti_2O_7$ and $Ho_2Ti_2O_7$), $a = 0.354$ nm is the nearest-neighbour distance between moments, and $\mathbf{r}_{ij}$ is the vector connecting sites i and j. Only six energetically degenerate ground-state spin configurations occur per tetrahedron[13], all of which have two spins pointing in and two pointing out (Fig. 1d). The magnetic monopole model of the spin ices is then achieved by rewriting the real Ising dipoles $\pm\mu$ of equation (1) in terms of magnetic charges $\pm m_*$ placed at the centres of adjacent tetrahedra such that $\pm\mu = \pm m_* d/2$ (Fig. 1d), where d is the distance between tetrahedron centres, r_α. Each centre is then labelled by a net magnetic charge m_α, where $m_\alpha = 0$ for the 2-in/2-out configuration, $m_\alpha = m_*$ for the 3-out/1-in configuration and $m_\alpha = -m_*$ for the 3-in/1-out configuration (Fig. 1d). The interaction potential between magnetic charges m_α and m_β at sites r_α and r_β is then represented by the Hamiltonian[6,9]

$$H = \frac{\mu_0}{4\pi}\sum_{\alpha<\beta}\frac{m_\alpha m_\beta}{r_{\alpha\beta}} + \frac{\nu}{2}\sum_\alpha m_\alpha^2 \tag{2}$$

where $\nu = (J/3) + 4D(1+\sqrt{2/3})/3$ and $r_{\alpha\beta}$ is the distance between r_α and r_β. In equation (2) the first term represents the Coulomb-like interactions between magnetic charges and the second term an on-site repulsion that enforces $m_\alpha = 0$, or a 2-in/2-out ground state, at $T = 0$. In this picture, when thermal fluctuations randomly flip a fraction of the Dy spins, magnetic monopole quasiparticles with charges $\pm m_*$ along with a small additional population[14] with charges $\pm 2m_*$ are generated. Overall, the low-energy spin excitations are then hypothesized to be a plasma of $\pm m_*$ magnetic charges[5,6,9,10] interacting via a Coulomb-like potential while undergoing rapid thermally activated GR across an energy barrier of $\Delta \approx 2\nu(\mu/d)^2$.

Thermally generated plasmas of $\pm e$ electric charges, subject to both Coulomb interactions and spontaneous GR, are well understood in intrinsic semiconductors[15–18]. Here, thermal GR of $\pm e$ pairs generates voltage noise with a spectral density of $S_V(\omega, T) = V^2 S_N(\omega, T)/N_0^2$, where $S_N(\omega, T)$ is the spectral number of GR fluctuations in the number N of $\pm e$ pairs, N_0 is their equilibrium number at a given temperature T, and ω is the angular frequency. Analogous theories for GR fluctuations in a plasma of $\pm m_*$ magnetic-charge pairs have recently been developed for spin ice compounds[7]. The rates of $\pm m_*$ pair generation, $g(N, T)$, and recombination, $r(N, T)$, are such that $g(N,T)|_{N_0} = r(N,T)|_{N_0}$ where $N_0(T)$ is the equilibrium number of $\pm m_*$

---

[1]Department of Physics, Cornell University, Ithaca, NY, USA. [2]Clarendon Laboratory, University of Oxford, Oxford, UK. [3]Department of Physics, Stanford University, Stanford, CA, USA. [4]Department of Physics, Technion – Israel Institute of Technology, Haifa, Israel. [5]Rudolf Peierls Centre for Theoretical Physics, Clarendon Laboratory, Oxford, UK. [6]Brockhouse Institute for Materials Research, McMaster University, Hamilton, Ontario, Canada. [7]Department of Physics, McMaster University, Hamilton, Ontario, Canada. [8]Canadian Institute for Advanced Research, Toronto, Ontario, Canada. [9]Department of Physics, University College Cork, Cork, Ireland. [10]These authors contributed equally: Ritika Dusad, Franziska K. K. Kirschner. *e-mail: stephen.blundell@physics.ox.ac.uk; jcseamusdavis@gmail.com

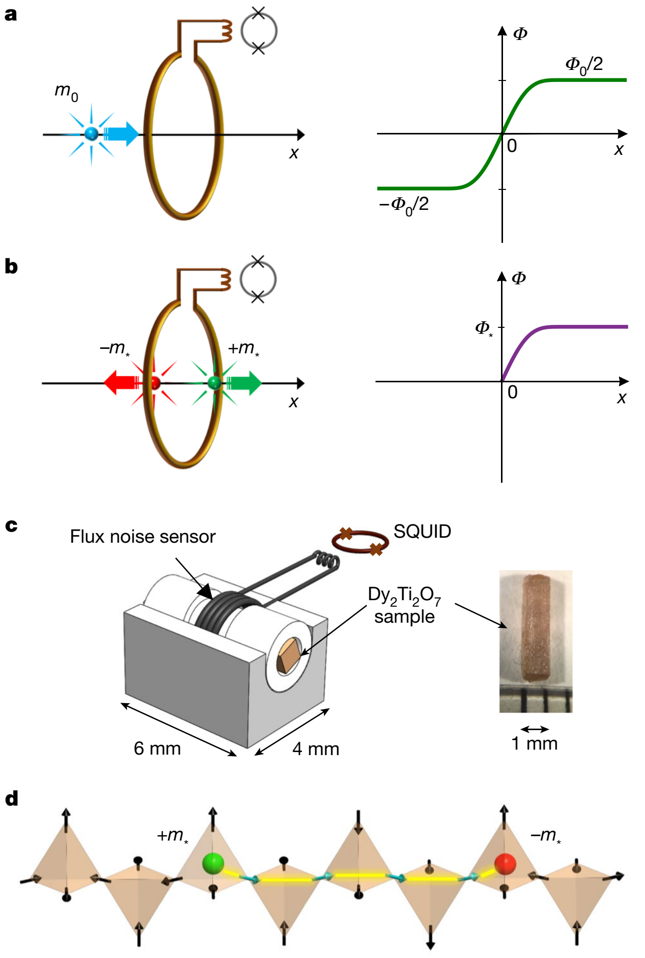

Fig. 1 | SQUID detection of quantized flux jump of magnetic monopoles. **a**, Schematic of a fundamental Dirac monopole with charge $m_0 = \pm h/(\mu_0 e)$ traversing the SQUID input coil from $x = -\infty$ to $x = +\infty$. The magnetic-flux threading of the SQUID changes in total by $\Phi_0 = h/e$. **b**, Schematic of two emergent magnetic charges $\pm m_*$ generated in $\mathrm{Dy_2Ti_2O_7}$ at $x = 0$ by a thermal fluctuation. As each charge departs in opposite directions towards $x = \pm\infty$, the net flux threading the SQUID changes in total by $\Phi_* = \mu_0 m_*$. The dark grey circles with two Xs denote the SQUID. **c**, Schematic of the SNS (see Methods section 'Spin noise spectrometer'). The primary coil, consisting of six turns of 0.09-mm-diameter NbTi wire wound on a cylindrical Macor shell, and the two wires connecting it to the input coil of a Quantum Design 550 DC SQUID are contained within a cylindrical superconducting Nb flux shield (not shown). The thermal conductivity of Macor is sufficient to thermalize the sample for any $T > 1$ K. Inset, single crystals of $\mathrm{Dy_2Ti_2O_7}$ cut in the shape of a rod with a square cross-section; the crystals are placed along the axis of the pickup coil. **d**. Schematic representation of the spin ice excited state in which two magnetic charges, $\pm m_*$, are generated by a spin flip and propagate through the material. In $\mathrm{Dy_2Ti_2O_7}$ the tetrahedron corners are the midpoints of the bonds of a diamond lattice defined by the centres of the tetrahedra, and all such bonds point along the local [111] direction. The ratio of the lattice constant of the diamond d and that of the fundamental pyrochlore lattice a is $d = \sqrt{3/(2a)}$. A single flip of an Ising Dy^{3+} spin converts the 2-in/2-out $m_\alpha = 0$ configuration in adjacent tetrahedra to a situation with adjacent $m_\alpha = m_*$ for the 3-out/1-in configuration in one tetrahedron and $m_\alpha = -m_*$ for the 3-in/1-out configuration in the next one. These two opposite magnetic charges can then separate via a sequence of spin flips in sequential tetrahedra, which leave them all in the 2-in/2-out $m_\alpha = 0$ configuration, except at the ends of this chain. However, owing to spin ice constraints, the specific path taken (which can be defined as a Dirac string with flux Φ_*) cannot be traversed sequentially by another magnetic charge of the same sign.

pairs. However, thermally stimulated fluctuations $\delta N = N - N_0$ in the number of $\pm m_*$ pairs occur owing to the GR processes. The Langevin equation for such fluctuations is[7]

$$\frac{\mathrm{d}(\delta \mathrm{N})}{\mathrm{d}t} = -\frac{\delta N}{\tau(T)} + \sqrt{A(T)}\,\zeta(t) \tag{3}$$

where the GR rate is $\tau(T) = \frac{1}{(\mathrm{d}r\,/\,\mathrm{d}N) - (\mathrm{d}g\,/\,\mathrm{d}N)}\Big|_{N_0}$ and $\sqrt{A(T)}\,\zeta(t)$ represents the thermally generated stimulus, which is uncorrelated in time[7,14]. Taking the Fourier transform of equation (3) yields the predicted spectral density of fluctuations in the number N of $\pm m_*$ pairs as[7]

$$S_N(\omega, T) = \frac{4\sigma_N^2 \tau(T)}{1 + \omega^2 \tau^2(T)} \tag{4}$$

where $\sigma_N^2 = \overline{(N - N_0)^2}$ is the variance. This result, shown schematically in Fig. 2a for a sequence of different $\tau(T)$ rates, reveals many intriguing properties. The spectral density of $\pm m_*$ pair fluctuations should be constant up to an angular frequency of $\omega_{\mathrm{GR}}(T) \approx 1/\tau_{\mathrm{GR}}(T)$ on the so-called GR noise plateau because of the randomness of the GR processes. Above this frequency, $S_N(\omega, T)$ should eventually fall off as $1/\omega^2$ for timescales on which uncorrelated magnetic monopoles can propagate freely. Another signature predicted by equation (4) for magnetic monopole GR processes is that, in a regime where σ_N^2 is approximately constant[7], the power spectral density of the low-frequency-number fluctuations, $S_N(\omega \to 0, T)$, should increase proportionately to $\tau(T)$.

However, a key challenge remains for the SQUID detection of emergent magnetic monopoles[6]: the GR fluctuations in the number of $\pm m_*$ pairs must be related directly to the fluctuations of the magnetic flux $\Phi(t)$ that is detectable by a SQUID (Fig. 1c). Moreover, equation (4) does not account for correlations in the motion of singly charged monopoles or for the existence of any doubly charged monopoles[14]. In theory, the correlations exist because of topological constraints that distinguish the dynamics of $\pm m_*$ pairs in spin ice from free particle–antiparticle pairs. Each co-generated $\pm m_*$ pair is connected by a Dirac string with magnetic flux $\Phi_* = m_* \mu_0$ (yellow trace in Fig. 1d), and the spin configuration within each Dirac string prevents sequential traversal along it by a second monopole of the same sign[10]. Therefore, a microscopic theory is required for magnetization fluctuations and noise, including the effects of both doubly charged monopoles and correlated monopole motion. Here we use Monte Carlo simulations of the thermally generated magnetic configurations described by equation (1) (see Methods section 'Monte Carlo simulations'; the calibration of the Monte Carlo time step is described in Methods section 'Calibration of Monte Carlo time step'). The result is a prediction of the spectral density of fluctuations $S_{M_z}(\omega, T)$ in the z component of the magnetization of $\mathrm{Dy_2Ti_2O_7}$ crystals for each ω and T. Figure 2b shows such Monte Carlo simulation data, presented as the predicted noise spectral density of magnetic-field fluctuations $S_{B_z}(\omega, T)$ for $\mathrm{Dy_2Ti_2O_7}$ crystals of volume approximately equal to that of our millimetre-scale samples. Because our samples are about 10^{16} times larger than the volumes that can be studied by Monte Carlo simulations, the absolute magnitude of $S_{B_z}(\omega, T)$ is an estimation (see Methods section 'Monte Carlo simulations') because the effects of finite-size scaling on DSI Monte Carlo simulations[19] over such a volume range are unknown. Nevertheless, these Monte Carlo simulations, which are based on equation (1), provide several important predictions. First, they reveal an analytical form of $S_{B_z}(\omega, T)$ (Fig. 2b) that is equivalent in key characteristics to equation (4) (Fig. 2a), as derived using the Langevin equation for GR fluctuations of $\pm m_*$ pairs. Second, by fitting the functional form $\tau(T)/\{1 + [\omega\tau(T)]^b\}$ to the Monte Carlo simulation data in Fig. 2b, one can determine $\tau(T)$. Third, the Monte Carlo simulation of $S_{B_z}(0, T)$ is approximately proportional to $\tau(T)$ for the temperature range of our experiments (Fig. 2c), once an offset to all $S_{B_z}(\omega, T)$ values is considered to account for numerical Nyquist (sampling) noise. Finally, the relationship $S(\omega) \propto \omega^{-2}$, which applies at high frequencies according to GR theory with a single GR time constant[7], is replaced with a more complex behaviour of $S(\omega) \propto \omega^{-b}$ with $b(T) < 2$. This effect may be due to a combination of noise spectral densities, as in equation (4), but with a distribution of GR time constants. In any case, as discussed below, the Monte Carlo simulations indicate that this $S(\omega) \propto \omega^{-b}$ behaviour in

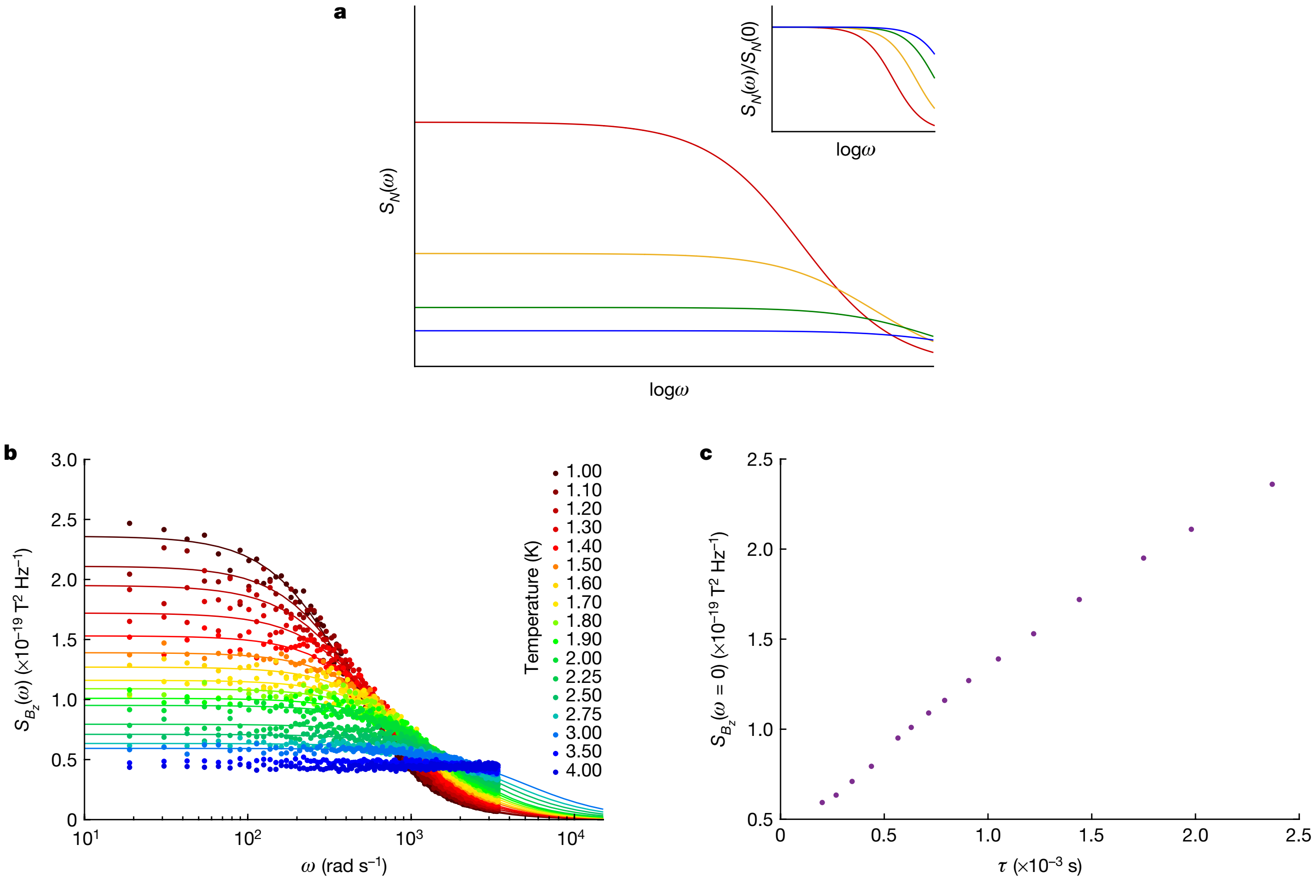

Fig. 2 | Spectral density of fluctuations in monopole number and magnetization. a, Spectral density of fluctuations in monopole number $S_N(\omega, T)$ predicted from equation (4) for several monopole GR time constants τ in the temperature range from 4 K to ~1 K, which one might expect to achieve by cooling $Dy_2Ti_2O_7$. The GR plateau in $S_N(\omega, T)$ for $\omega \rightarrow 0$ is clear, as is the ω^{-2} fall-off expected of free-monopole motion for frequencies $\omega\tau > 1$. The inset shows the normalized spectral density, $S_N(\omega, T)/S_N(0, T)$. The colour scale is as in **b**. **b**, Spectral density of magnetic-field fluctuations $S_{B_z}(\omega, T)$ in the $Dy_2Ti_2O_7$ sample, predicted by Monte Carlo simulations using the Hamiltonian of equation (1) in the temperature range $1\ \text{K} \leq T \leq 4\ \text{K}$. These simulations are physically distinct from those reported in ref. [8] because here we focus on bulk fluctuations of the z component of magnetization, $M_z(t)$, or of the associated z component of the magnetic field, $B_z(t)$, whereas ref. [8] considers field fluctuations in vacuum outside a specific crystal termination surface. Because of the periodic boundary conditions and the very small Monte Carlo sample volume, the scaling of the predicted magnitude of $S_{B_z}(\omega, T)$ for the Monte Carlo sample to the absolute magnitude expected for an experimental sample of volume about 10^{16} times greater is an approximation (see Methods section 'Monte Carlo simulations'). However, this does not affect the form of $S_{B_z}(\omega, T)$ expected for a macroscopic experimental sample. **c**, Relationship between $S_{B_z}(0, T)$ and $\tau(T)$ for the GR fluctuations of a $\pm m_*$ magnetic-charge plasma, as predicted by $Dy_2Ti_2O_7$ Monte Carlo simulations[8] of $B_z(t)$. We note that all of the $S_{B_z}(0, T)$ data points are offset by a constant along the vertical axis owing to artefacts of Nyquist (sampling) noise at the high-frequency end of the Monte Carlo calculations.

$Dy_2Ti_2O_7$ derives microscopically from topological constraints due to the Dirac strings, causing the motion of interacting monopoles to become correlated.

These theoretical innovations provide clear predictors for the magnetic-flux noise spectral density $S_\Phi(\omega, T)$ due to a plasma of $\pm m_*$ magnetic charges undergoing GR processes. First, random fluctuations dominate at frequencies $\omega\tau(T) \ll 1$ and topologically constrained monopole dynamics dominate at $\omega\tau(T) \gg 1$, with a transition regime surrounding $\omega\tau(T) \approx 1$. Second, even though the evolution of magnetic relaxation times with T is microscopically complex[10], the GR prediction for a plasma of $\pm m_*$ magnetic charges is that

$$S_\Phi(0, T) \propto \tau(T) \tag{5}$$

provided that σ_N^2 remains approximately constant in the temperature range of the experiment (see ref. [7] and Methods section 'Statistics of monopole number fluctuations'). Third, signatures of topological constraints on monopole dynamics are contained within the prediction for the magnetic-flux noise autocorrelation function and power-law exponent $b(T)$. The combined conclusions from the Monte Carlo simulations of magnetization noise in $Dy_2Ti_2O_7$ (Fig. 2b) are embodied in

$$S_\Phi(\omega, T) \propto \frac{\tau(T)}{1 + [\omega\tau(T)]^b} \tag{6}$$

To explore these prospects, we developed a high-sensitivity SQUID-based flux noise spectrometer[20,21] to measure the $S_\Phi(\omega, T)$ of crystalline samples. Here we use it for studies of $Dy_2Ti_2O_7$ over the frequency range $1\ \text{Hz} < f < 2.5\ \text{kHz}$ (see Methods section 'Spin noise spectrometer'). This spin noise spectrometer (SNS) is mounted on a custom-built, low-vibration cryostat operable in the range $1.2\ \text{K} \leq T \leq 7\ \text{K}$, which was estimated to be optimal for detection of the most intense flux noise spectra from the millimetre-scale $Dy_2Ti_2O_7$ crystals studied. Measurements consist of: varying the temperature of the sample assembly from 1.2 K to 4 K in steps of 25 mK, using the SQUID to measure the magnetic flux $\Phi(t)$ generated by the $Dy_2Ti_2O_7$ sample at each T and utilizing a spectrum analyser to determine the flux noise spectral density $S_\Phi(\omega, T)$.

Figure 3a shows a typical example of $S_\Phi(\omega, T)$ measured from $Dy_2Ti_2O_7$ samples in our SNS at $1.2\ \text{K} \leq T \leq 4\ \text{K}$. The left-hand axis is the magnetic-flux noise spectral density $S_\Phi(\omega, T)$ and the right-hand axis shows an estimate of the equivalent magnetic-field noise spectral density $S_{B_z}(\omega, T)$ within the $Dy_2Ti_2O_7$ samples (see Methods section

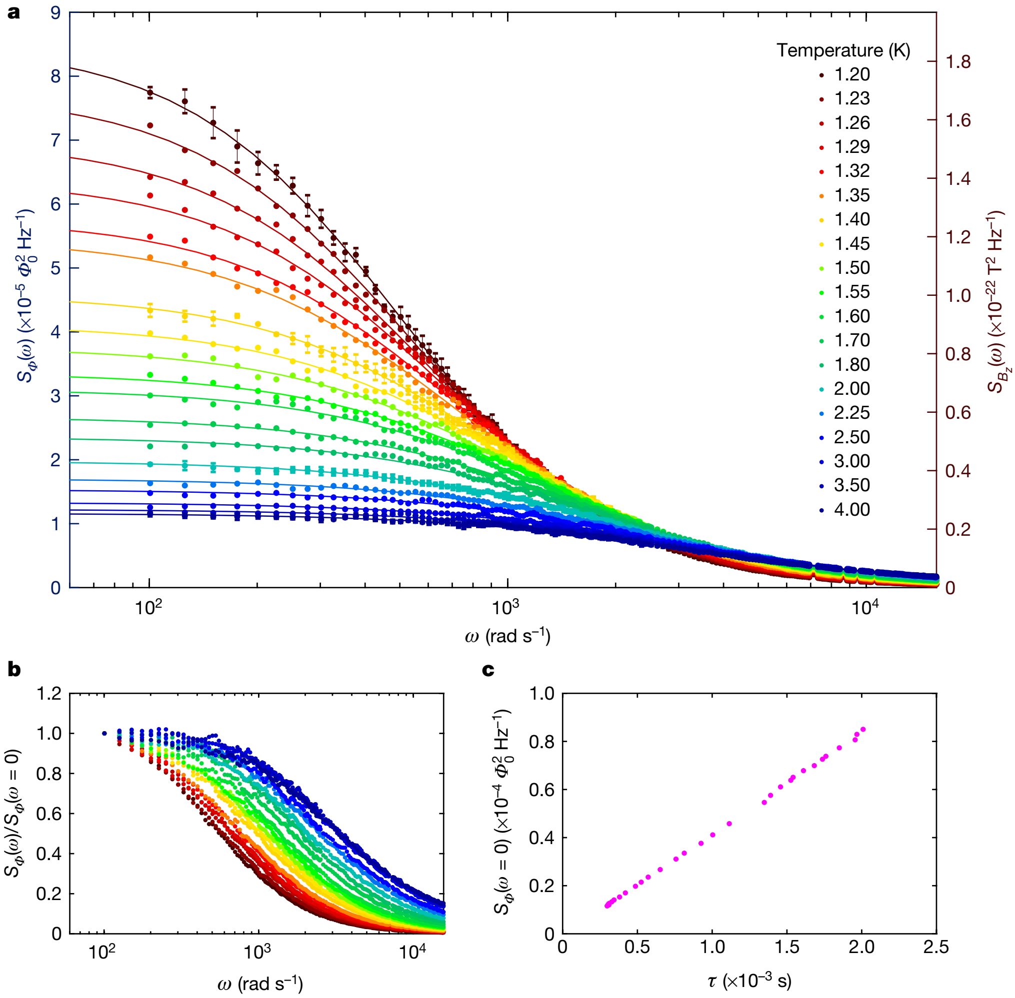

Fig. 3 | Spectral density of magnetic-flux noise in $Dy_2Ti_2O_7$. **a**, Measured spectral density of flux noise $S_\Phi(\omega, T)$ from $Dy_2Ti_2O_7$ samples (for example, Fig. 1c) in the range $1.2\ \mathrm{K} \le T \le 4\ \mathrm{K}$. The left-hand axis is the magnetic-flux noise spectral density $S_\Phi(\omega, T)$; the right-hand axis is an estimate of the equivalent magnetic-field noise spectral density $S_{B_z}(\omega, T)$ averaged over the $Dy_2Ti_2O_7$ samples (on the basis of the calibration of the flux sensitivity of the spectrometer; see Methods section 'Spin noise spectrometer'). The best fits of $S_{B_z}(\omega, T)$ to the functional form $\tau(T)/\{1+[\omega\tau(T)]^{b(T)}\}$ are shown as solid curves. Overall we find the $S_\Phi(\omega, T)$ of $Dy_2Ti_2O_7$ to be constant for frequencies 1 Hz $\lesssim f \lesssim 2\pi/\tau(T)$ Hz, above which it falls off as ω^b. Error bars (shown only for four temperatures—1.20 K, 1.40 K, 2.00 K and 4.00 K—for visual clarity) represent the standard deviation of each data point, extracted from an average of five independent $Dy_2Ti_2O_7$ flux noise datasets at each temperature. **b**, Normalized flux noise spectral density $S_\Phi(\omega, T)/S_\Phi(0, T)$, revealing the divergence of the time constant $\tau(T)$ towards longer times at lower temperatures (Extended Data Fig. 5). **c**, $S_\Phi(0, T)$ plotted versus $\tau(T)$ as measured from fitting the data in Fig. 3a. The results demonstrate that $S_\Phi(0, T) \propto \tau(T)$ for $Dy_2Ti_2O_7$ throughout this temperature range, as expected for $\pm m_*$ GR magnetic-flux noise.

'Spin noise spectrometer'). Each dataset is fitted with equation (6), with the best fit shown as a solid curve (see Methods section 'Data analysis'). Thus, we find that the magnetic-flux noise spectral density of $Dy_2Ti_2O_7$ is constant for frequencies from near 1 Hz up to an angular frequency of $\omega(T) \approx 1/\tau(T)$, above which it falls off as ω^{-b}, where b spans the range 1.2–1.5. Figure 3b shows $S_\Phi(\omega, T)/S_\Phi(0, T)$, revealing that the GR time constant $\tau(T)$ evolves rapidly towards longer times at lower T. Figure 3c shows the measured $S_\Phi(0, T)$ from Fig. 3a plotted against the $\tau(T)$ measured from the fits to $S_\Phi(\omega, T)$ in Fig. 3a, where T is the implicit variable and ranges from 1.2 K to 4 K. Here we see that $S_\Phi(0, T)$ is proportional to $\tau(T)$ throughout our temperature range (Figs. 2c, 4a). This situation is as expected from GR models when the variance in monopole number σ_N^2 remains roughly constant, as confirmed in Methods section 'Data analysis'. Comparison of GR time constants $\tau(T)$ derived from flux noise spectroscopy to magnetic relaxation times $\tau_M(T)$ derived from magnetic susceptibility measurements[22–25] reveal them to have good empirical correspondence (see Methods section 'Data analysis'), although their microscopic relationship remains to be identified precisely. Generally, the theoretical predictions for a thermally generated plasma of $\pm m_*$ magnetic charges that is dominated by GR fluctuations (Fig. 2) are consistent with all of these unusual magnetic-flux noise phenomena (Figs. 3, 4a). Finally, because the monopole times $\tau(T)$ are in the millisecond range, magnetic monopole flux noise amplified by the SQUID is actually audible to humans (see Supplementary Video 1).

The frequency dependence of $S_\Phi(\omega, T)$ contains additional key information. We used our Monte Carlo simulations for $Dy_2Ti_2O_7$ to predict the autocorrelation function $C_{B_z}(t, T)$ of magnetic-field fluctuations $B_z(t)$. Figure 4b shows the Monte Carlo predictions for $\log[C_{B_z}(t, T)/C_{B_z}(0, T)]$ at $T = 1.2$ K for three distinct theories of magnetic monopole dynamics. The first model (blue) describes a $\pm m_*$ magnetic-charge plasma of DSI with Coulomb-like interactions and Dirac-strings[8,10] (yellow line in Fig. 1d). The second model (green) is the nearest-neighbour spin ice model (NNSI), in which Coulomb-like interactions are suppressed but Dirac-string constraints are present. The final model (red) is a neutral plasma of $\pm m_*$ magnetic charges undergoing Coulomb interactions that is topologically unconstrained. For comparison our measured autocorrelation function $\log[C_{B_z}(t, T)/C_{B_z}(0, T)]$ is plotted (black) in Fig. 4b with a best-fit curve overlaid. Clearly, the DSI model of equation (1), which includes

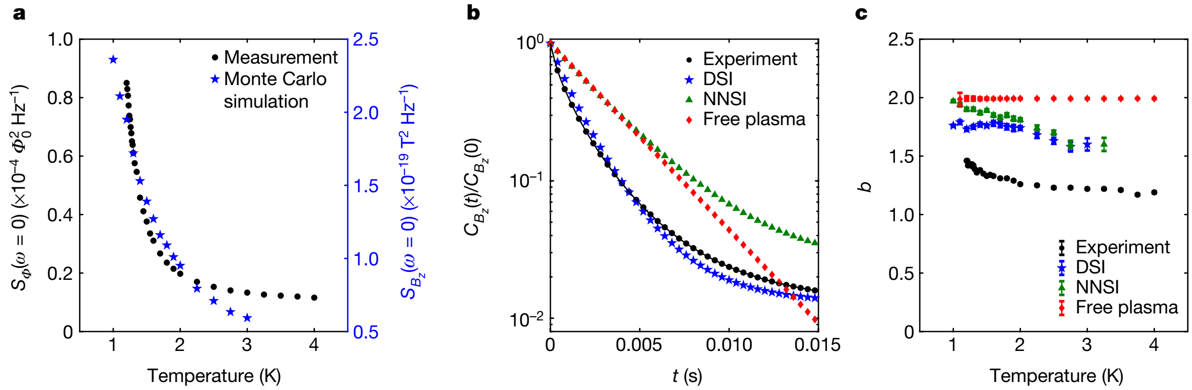

Fig. 4 | Spectral density of magnetic-flux noise for a correlated monopole fluid. a, Measured (black circles) and Monte Carlo predicted (blue stars) low-frequency noise spectral density, $S_\Phi(0, T)$, of $Dy_2Ti_2O_7$ as a function of temperature. **b**, Monte Carlo predictions of the autocorrelation function $\log[C_{B_z}(t)/C_{B_z}(0)]$ for field fluctuations $B_z(t)$ at $T = 1.2$ K, obtained using three spin dynamics models for $Dy_2Ti_2O_7$. The DSI model (blue) contains Coulomb-like interactions and constraints imposed by Dirac strings on the repeated passage of same-sign monopoles along the same trajectory. The NNSI model has the Coulomb interactions suppressed (green). The free-monopole plasma model (red) is based on free-monopole GR theory. The measured autocorrelation function $\log[C_{B_z}(t)/C_{B_z}(0)]$ of magnetic-field fluctuations $B_z(t)$ of $Dy_2Ti_2O_7$ is plotted as black dots and overlaid with a fitting function (black line). Clearly, the autocorrelation function of the DSI model corresponds best to the measured $C_{B_z}(t)$. We note that the difference between the single-slope $C_{B_z}(t)$ obtained for the free-monopole plasma[7] and the more complex shapes predicted by the other models represents microscopically the distinction between a simple process involving a single relaxation time constant and a more complex one, which potentially involves a range of relaxation time constants. Most importantly, the measured $C_{B_z}(t)$ shows that magnetization dynamics is obviously strongly correlated in time. **c**, Predictions of the exponent $b(T)$ when $S_{B_z}(\omega, T)$ (as determined from the Monte Carlo simulations for the three magnetic-charge dynamics models) is fitted to the functional form $\tau(T)/\{1 + [\omega\tau(T)]^{b(T)}\}$. The measured $b(T)$, obtained by fitting $S_{B_z}(\omega, T)$ (as determined from the experimental data in Fig. 3a) to the functional form $\tau(T)/\{1 + [\omega\tau(T)]^{b(T)}\}$, is shown in black. The time constants $\tau(T)$ of the predicted $S_{B_z}(\omega, T)$ and the measured $S_\Phi(\omega, T)$ are not free parameters here (Fig. 4a). Error bars represent the uncertainty in the analytical fits to the data due to statistical fluctuations of $S_\Phi(\omega, T)$.

Coulomb-like interactions and Dirac-string topological constraints, is far more consistent with the directly measured correlation function in this system. Moreover, the NNSI model is inconsistent with the experimental results, as short-time correlations appear to be completely absent. This correlation function phenomenology is virtually unchanged, except for values of $\tau(T)$, within our temperature range. The Monte Carlo predictions of the frequency exponent b from the same three models can be determined by fitting each simulated $S_{B_z}(\omega, T)$ to $\tau(T)/\{1+[\omega\tau(T)]^{b(T)}\}$. These results for $b(T)$ are shown in Fig. 4c, along with the measured $b(T)$, as determined by fitting the same function to each measured $S_{B_z}(\omega, T)$. Here we see that the GR theory expressed by equation (4) is well supported by the Monte Carlo simulations, which predict $S_\Phi(\omega, T) \propto \tau/[1+(\omega\tau)^b]$, where $b = 2$ for uncorrelated free monopoles and $b < 2$ for the full DSI Hamiltonian. Moreover, comparison between simulated and measured autocorrelation functions $C_{B_z}(t, T)$ and fall-off exponents b for magnetic-flux noise in $Dy_2Ti_2O_7$ reveals that the DSI model is the most consistent with the observed phenomenology. To achieve more precise agreement may require fine adjustment of J or D in equation (1)[26] or better control over finite-size scaling effects[19]. Overall, however, Fig. 4c implies that the power-law signatures of strong correlations observed in both $\log[C_{B_z}(t, T)/C_{B_z}(0, T)]$ and $S_{B_z}(\omega, T)$ are due to the combined effect of the Dirac string connecting each $\pm m_*$ pair (Fig. 1d) and the Coulomb interactions between all monopoles.

To recapitulate, theoretical predictions for the magnetic-flux signature of $\pm m_*$ magnetic charges in spin ice[6–8] are studied for the case of $Dy_2Ti_2O_7$. The intense magnetization noise predicted by Monte Carlo simulations (Fig. 2) was observed for the first time (Fig. 3a). The frequency and temperature dependence of the magnetic-flux noise spectrum $S_\Phi(\omega, T)$ predicted for $\pm m_*$ magnetic charges undergoing thermal GR (Fig. 2b, c) was confirmed directly and in detail (Fig. 3). The expected transition from a plateau of constant magnetic-flux noise[7,8] (for $\omega\tau(T) \ll 1$) to a power-law fall-off[8] (for $\omega\tau(T) \gg 1$) was observed throughout (Fig. 3a). Moreover, falling temperatures cause the low-frequency flux noise spectral density to increase rapidly as $S_\Phi(0, T) \propto \tau(T)$ (Fig. 4a). These characteristics are distinct from the magnetization noise spectral density signatures of a ferromagnet[20], a classic spin glass[21] or an Ising paramagnet[27], all of which evolve qualitatively differently with ω and T. On the other hand, within the context of both $\pm m_*$ GR theory[7] and Monte Carlo simulations for DSI[8], the observed $S_\Phi(\omega, T)$ (Figs. 3, 4) is consistent with other studies that imply that $Dy_2Ti_2O_7$ and $Ho_2Ti_2O_7$ contain a plasma of emergent magnetic monopoles[9,10,14,28–33]. Additionally, the agreement of the measured magnetization noise autocorrelation functions $C_{B_z}(t)/C_{B_z}(0)$ with those predicted from Monte Carlo simulations of equation (1) (Fig. 4b) implies substantial correlations in the motions of $\pm m_*$ magnetic charges in $Dy_2Ti_2O_7$. Overall, we found robust agreement between current theories for thermal GR of $\pm m_*$ pairs in a correlated magnetic monopole plasma (Fig. 2) and the phenomenology of the magnetic-flux noise spectral density in $Dy_2Ti_2O_7$ (Figs. 3, 4).

Online content

Any methods, additional references, Nature Research reporting summaries, source data, statements of data availability and associated accession codes are available at https://doi.org/10.1038/s41586-019-1358-1.

Received: 30 October 2018; Accepted: 29 April 2019;
Published online 3 July 2019.

1. Dirac, P. Quantised singularities in the electromagnetic field. *Proc. R. Soc. Lond. A* **133**, 60–72 (1931).
2. Hooft, G. Magnetic monopoles in unified gauge theories. *Nucl. Phys. B* **79**, 276–284 (1974).
3. Polyakov, A. M. Particle spectrum in the quantum field theory. *J. Exp. Theor. Phys. Lett.* **20**, 194–195 (1974).
4. Cabrera, B. First results from a superconductive detector for moving magnetic monopoles. *Phys. Rev. Lett.* **48**, 1378–1381 (1982).
5. Ryzhkin, I. A. Magnetic relaxation of rare-earth pyrochlores. *J. Exp. Theor. Phys.* **101**, 481–486 (2005).
6. Castelnovo, C., Moessner, R. & Sondhi, S. L. Magnetic monopoles in spin ice. *Nature* **451**, 42–45 (2008).
7. Klyuev, A., Ryzhkin, M. & Yakimov, A. Statistics of fluctuations of magnetic monopole concentration in spin ice. *Fluct. Noise Lett.* **16**, 1750035 (2017).
8. Kirschner, F. K. K., Flicker, F., Yacoby, A., Yao, N. & Blundell, S. J. Proposal for the detection of magnetic monopoles in spin ice via nanoscale magnetometry. *Phys. Rev. B* **97**, 140402 (2018).
9. Castelnovo, C., Moessner, R. & Sondhi, S. Spin ice, fractionalization, and topological order. *Annu. Rev. Condens. Matter Phys.* **3**, 35–55 (2012).

10. Jaubert, L. & Holdsworth, P. Magnetic monopole dynamics in spin ice. *J. Phys. Condens. Matter* **23**, 164222 (2011).
11. Rosenkranz, S. et al. Crystal-field interaction in the pyrochlore magnet $Ho_2Ti_2O_7$. *J. Appl. Phys.* **87**, 5914–5916 (2000).
12. den Hertog, B. & Gingras, M. Dipolar interactions and the origin of spin ice in Ising pyrochlore magnets. *Phys. Rev. Lett.* **84**, 3430–3433 (2000).
13. Ramirez, A., Hayashi, A., Cava, R., Siddharthan, R. & Shastry, B. Zero-point entropy in ‘spin ice’. *Nature* **399**, 333–335 (1999).
14. Kaiser, V. et al. Emergent electrochemistry in spin ice: Debye–Hückel theory and beyond. *Phys. Rev. B* **98**, 144413 (2018).
15. Burgess, R. E. The statistics of charge carrier fluctuations in semiconductors. *Proc. Phys. Soc. B* **69**, 1020–1027 (1956).
16. van Vliet, K. M. & Fassett, J. R. *Fluctuation Phenomena in Solids* (ed. Burgess, R. E.) (Academic Press, 1965).
17. Mitin, V., Reggiani, L. & Varani, L. in *Noise and Fluctuations Control in Electronic Devices* Ch. 2 (American Scientific Publishers, 2002).
18. Konczakowska, A. & Wilamowski, B. M. in *Fundamentals of Industrial Electronics* Ch. 11 (Taylor and Francis, 2011).
19. Melko, R. G. & Gingras, M. J. P. Monte Carlo studies of the dipolar spin ice model. *J. Phys. Condens. Matter* **16**, 1277–1319 (2004).
20. Vitale, S., Cavalleri, A., Cerdonio, M., Maraner, A. & Prodi, G. A. Thermal equilibrium noise with $1/f$ spectrum in a ferromagnetic alloy: anomalous temperature dependence. *J. Appl. Phys.* **76**, 6332–6334 (1994).
21. Reim, W., Koch, R., Malozemoff, A., Ketchen, M. & Maletta, H. Magnetic equilibrium noise in spin-glasses: $Eu_{0.4}Sr_{0.6}S$. *Phys. Rev. Lett.* **57**, 905–908 (1986).
22. Snyder, J. et al. Low-temperature spin freezing in the $Dy_2Ti_2O_7$ spin ice. *Phys. Rev. B* **69**, 064414 (2004).
23. Matsuhira, K. et al. Spin dynamics at very low temperature in spin ice $Dy_2Ti_2O_7$. *J. Phys. Soc. Jpn* **80**, 123711 (2011).
24. Yaraskavitch, L. R. et al. Spin dynamics in the frozen state of the dipolar spin ice material $Dy_2Ti_2O_7$. *Phys. Rev. B* **85**, 020410 (2012).
25. Kassner, E. R. et al. Supercooled spin liquid state in the frustrated pyrochlore $Dy_2Ti_2O_7$. *Proc. Natl Acad. Sci. USA* **112**, 8549 (2015).
26. Fennell, T. et al. Neutron scattering investigation of the spin ice state in $Dy_2Ti_2O_7$. *Phys. Rev. B* **70**, 134408 (2004).
27. Quilliam, J. A., Meng, S., Mugford, C. G. A. & Kycia, J. B. Evidence of spin glass dynamics in dilute $LiHo_xY_{1-x}F_4$. *Phys. Rev. Lett.* **101**, 187204 (2008).
28. Morris, D. et al. Dirac strings and magnetic monopoles in the spin ice $Dy_2Ti_2O_7$. *Science* **326**, 411–414 (2009).
29. Bramwell, S. T. et al. Measurement of the charge and current of magnetic monopoles in spin ice. *Nature* **461**, 956–959 (2009).
30. Bovo, L., Bloxsom, J., Prabhakaran, D., Aeppli, G. & Bramwell, S. Brownian motion and quantum dynamics of magnetic monopoles in spin ice. *Nat. Commun.* **4**, 1535–1542 (2013).
31. Giblin, S., Bramwell, S., Holdsworth, P., Prabhakaran, D. & Terry, I. Creation and measurement of long-lived magnetic monopole currents in spin ice. *Nat. Phys.* **7**, 252–258 (2011).
32. Kaiser, V., Bramwell, S. T., Holdsworth, P. C. W. & Moessner, R. ac Wien effect in spin ice, manifest in nonlinear, nonequilibrium susceptibility. *Phys. Rev. Lett.* **115**, 037201 (2015).
33. Paulsen, C. et al. Experimental signature of the attractive Coulomb force between positive and negative magnetic monopoles in spin ice. *Nat. Phys.* **12**, 661–666 (2016).

Acknowledgements We are grateful to C. Castelnovo, J. Goff, Y. B. Kim, M. J. Lawler, A. Ramirez, D. Schlom and N. Y. Yao for discussions and communications. J.C.S.D. thanks O. H. S Davis for discussions and for proposing to study magnetic noise in pyrochlores. R.D. thanks Y. X. Chong for assistance during experimental operations and acknowledges use of the Cornell Center for Materials Research Shared Facilities, supported through the NSF MRSEC programme (DMR-1719875). A.E. acknowledges support via Israeli Pazy Equipment Grant 299/18. F.K.K.K. acknowledges support from Lincoln College, Oxford. F.F. acknowledges support from the Astor Junior Research Fellowship of New College, Oxford. S.J.B. acknowledges support from EPSRC (EP/N023803/1). The conceptual design of our experimental techniques was supported by the W. M. Keck Foundation. J.C.S.D. acknowledges support from Science Foundation Ireland under Award SFI 17/RP/5445 and from the European Research Council (ERC) under award DLV-788932. R.D. and J.C.S.D. acknowledge support, plus funding for instrument development and experimental studies, from the Gordon and Betty Moore Foundation’s EPiQS Initiative through grant GBMF4544.

Author contributions R.D. and J.C.S.D. conceptualized the project and designed the experimental setup. R.D. developed the flux noise spectrometer. R.D., J.C.H., B.R.R. and A.E. carried out the experiments and data analysis. G.M.L. synthesized the $Dy_2Ti_2O_7$ samples. F.K.K.K. carried out the Monte Carlo simulations with help from F.F. G.M.L., S.J.B. and J.C.S.D. supervised the investigation and wrote the paper with key contributions from R.D., F.K.K.K. and F.F. The manuscript reflects the contributions of all authors.

Competing interests The authors declare no competing interests.

Additional information

Extended data is available for this paper at https://doi.org/10.1038/s41586-019-1358-1.
Supplementary information is available for this paper at https://doi.org/10.1038/s41586-019-1358-1.
Reprints and permissions information is available at http://www.nature.com/reprints.
Correspondence and requests for materials should be addressed to S.J.B. or J.C.S.D.

METHODS

Monte Carlo simulations. *Monte Carlo simulation procedures.* Monte Carlo (MC) simulations are used to model the magnetization dynamics of $Dy_2Ti_2O_7$. In general, these simulations are carried out on a sample containing $4\times4\times4$ unit cells, each of which contains 16 Dy^{3+} ions; we refer to this as the MC sample. Standard MC procedures are used[34], consisting of 10^6 cooling steps followed by an interval W of 5,000 MC time steps at fixed T, during which the time dependence of the net z component of the magnetic moment, $\mu_z(t)$, of the whole MC sample is simulated. This procedure is repeated 600 times. Carrying out the MC simulations for 5,000 sequential time steps ensures the capture of the range of magnetization dynamics timescales that is expected in this material at each temperature; these span from about 100 μs (for a single MC step) to approximately 1 s (the total time of the simulation). The temperature range of the simulations is 1.0–4.0 K. Because this is a simulation of bulk magnetization dynamics, periodic boundary conditions are used in all directions.

For a given configuration, the z component of the magnetic moment of the MC sample, μ_z, is found by summing the z components of the magnetic moments of the 1,024 Dy ions that it contains. The magnitude of the magnetic moment for each Dy Ising spin is $\mu\approx10\mu_B$. The MC simulated time dependence of this value at a given temperature T, $\mu_z(t,T)$, is evaluated sequentially throughout the whole time window W. Its autocorrelation function is then

$$C_{\mu_z}(\tau,T)=\frac{1}{W}\int_{-W/2}^{W/2}\mu_z(t,T)\mu_z(t+\tau,T)\mathrm{d}t \tag{7}$$

(in units of μ_B^2). The predicted spectral density of magnetic-moment noise in the MC sample is then calculated using the Wiener–Khinchin theorem

$$S_{\mu_z}(\omega,T)=4\int_0^{\infty}C_{\mu_z}(\tau,T)\cos(\omega\tau)\mathrm{d}\tau \tag{8}$$

expressed in $\mu_B^2\times(\mathrm{MC\ step})$. We extract the frequency range 10^{-4} (MC steps)$^{-1}$ to 10^{-1} (MC steps)$^{-1}$ with a Nyquist frequency of 0.5 (MC steps)$^{-1}$. Equation (8) is then averaged over the 600 independent simulation runs to get better precision for $S_{\mu_z}(\omega,T)$. Finally, the time axis of the MC simulation is converted from MC steps to seconds as described in Methods section 'Calibration of Monte Carlo time step', so that the angular frequency in equation (8) and the following equations is $\omega=2\pi/t$ rad s^{-1} and $S_{\mu_z}(\omega,T)$ is expressed in μ_B^2 s.

To convert to the noise spectral density of the z component of the magnetization in SI units, we use $S_{M_z}(\omega,T)=C_0^2S_{\mu_z}(\omega,T)/V^2$ (in $A^2\ m^{-2}$ s), where $V=6.6\times10^{-26}\ m^3$ is the volume of the MC sample and $C_0=9.27\times10^{-24}\ A\ m^2\mu_B^{-1}$. To estimate the predicted spectral density of the z-magnetization noise expected from the experimental $Dy_2Ti_2O_7$ sample within the range of the SQUID pickup coil (Fig. 1c), we approximate that there are $n=2.9\times10^{16}\pm20\%$ MC samples in the pickup coil volume and divide $S_{M_z}(\omega,T)$ by n. The predicted spectral density of fluctuations of the z component of the magnetic field B (in tesla) within the sample is then given by

$$S_{B_z}(\omega,T)=\mu_0^2S_{M_z}(\omega,T) \tag{9}$$

(in T^2 s). Figure 2b shows this estimation of $S_{B_z}(\omega,T)$ from the MC simulation of the DSI Hamiltonian (equation (1)) for our specific sample geometry in the SNS.

Model Hamiltonians. First, the full DSI Hamiltonian (given in equation (1)) is employed. The exchange energy is $J\approx-3.72$ K and the dipolar energy is $D\approx1.41$ K for $Dy_2Ti_2O_7$. This DSI model leads to the lowest energy state of Dy spins pointing to the centre or out of the tetrahedron on which they are sitting along the local <111> axes. This state is known as the 2-in/2-out state (Fig. 1d). As previously discussed, the violation of this rule by a spin flip causes the generation of a monopole–anti-monopole pair with charge $\pm m_*$ or a doubly charged pair with charge $\pm2m_*$ (ref. [14]). The energy of two nearest-neighbour monopoles is 3.06 K, and the energy required to create one monopole is $\Delta=4.35$ K.

Second, the NNSI Hamiltonian is considered by setting $D=0$ in equation (1), which suppresses the effects of long-range Coulomb interactions. J is chosen such that the system still has a 2-in/2-out ground state while having the same density of excitations as DSI at a given temperature. This system still has monopole-like excitations, but the force between the monopoles is greatly reduced. Thus, we calculate the noise spectral density of $\pm m_*$ magnetic charge pairs hopping in the presence of strongly suppressed Coulomb interactions.

Third, we identify the noise spectrum of $\pm m_*$ magnetic charge pairs hopping freely in the absence of Coulomb interactions or topological constraints due to Dirac strings in $Dy_2Ti_2O_7$. The model is described by equation (2), with the m_* charges located on the sites of a diamond lattice.

Statistics of monopole number fluctuations. The master equation for generation $g(N,T)$ and recombination $r(N,T)$ of magnetic monopole pairs[7] defines the probability $P(N,T)$ of finding N monopole pairs at temperature T in a steady-state condition

$$\begin{aligned}\frac{\mathrm{d}P(N,T)}{\mathrm{d}t}&=r(N+1,T)P(N+1,T)+g(N-1,T)P(N-1,T)\\&\quad-P(N,T)[g(N,T)+r(N,T)]=0\end{aligned} \tag{10}$$

Here $g(N,T)$ and $r(N,T)$ are the generation and recombination rates of the monopoles, respectively, and one $\pm m_*$ pair per generation or recombination event is added or removed, correspondingly. The exact dependence of g and r on N and T depends on the microscopic dynamics of the GR processes in the system under investigation. We also note that[15,16]

$$\frac{\mathrm{d}(\delta N)}{\mathrm{d}t}=-\delta N\left.\frac{\mathrm{d}(r-g)}{\mathrm{d}N}\right|_{N=N_0} \tag{11}$$

where $\delta N=N-N_0$. The time constant required for N to approach its equilibrium value is defined as

$$\frac{1}{\tau(T)}=\left.\frac{\mathrm{d}(r-g)}{\mathrm{d}N}\right|_{N_0}=r'(N_0,T)-g'(N_0,T) \tag{12}$$

Obviously, in equilibrium, $g(N_0,T)=r(N_0,T)$.

Expanding $\ln P(N,T)$ about its maximum value $\ln P(N_0,T)$ in a quadratic fashion[15,16] yields

$$\left[\frac{\partial^2}{\partial N^2}\ln P(N,T)\right]_{N=N_0}=\frac{g'(N_0,T)}{g(N_0,T)}-\frac{r'(N_0,T)}{r(N_0,T)} \tag{13}$$

so that

$$\ln P(N,T)=\ln P(N_0,T)-\frac{1}{2}(N-N_0)^2\left[\frac{r'(N_0,T)}{r(N_0,T)}-\frac{g'(N_0,T)}{g(N_0,T)}\right] \tag{14}$$

Thus the expected Gaussian probability distribution of N about its most probable value, N_0, is

$$P(N,T)=P(N_0,T)\exp\left[-\frac{(N-N_0)^2}{2\sigma_N^2}\right] \tag{15}$$

The variance of the monopole number $\sigma_N^2=\overline{(N-N_0)^2}$ is then determined from equations (13), (15)[15,16] as

$$\sigma_N^2(T)=\left[\frac{r'(N_0,T)}{r(N_0,T)}-\frac{g'(N_0,T)}{g(N_0,T)}\right]^{-1}=\frac{g(N_0,T)}{r'(N_0,T)-g'(N_0,T)}=g(N_0,T)\tau(T) \tag{16}$$

For emergent magnetic monopoles in $Dy_2Ti_2O_7$, the equilibrium generation rate at temperature T within our range will be $g(N_0,T)\propto\exp(-\Delta/T)$ where Δ is the thermal energy barrier for thermal spin flips that generate the monopoles. It has been established[23] from previous experiments that at these higher temperatures the time constants are given by $\tau(T)\approx\exp(\Delta/T)$. This implies that the variance of the magnetic monopole number $\sigma_N^2\approx\exp(\Delta/T)\exp(-\Delta/T)$ would be expected to be approximately constant in this temperature range.

Spin noise spectrometer. *Design.* We use a custom-built 1-K cryostat to carry out our experiments, with the SQUID, the sample-holder and their superconducting shielding mounted below the refrigerator. The SNS setup consists of a cylindrical sample-holder with a concentric hole of diameter 1.4 mm and length 5.7 mm, which is used to encapsulate the rod-shaped samples as shown in Fig. 1c. The superconducting pickup coil is wound around the sample-holder and consists of 6 turns of thin Nb wire with inductance $L\approx0.25$ μH. The input inductance of the QD 550 SQUID is reported by the manufacturer (Quantum Design) as 2.0 μH. The sample-holder and the SQUID circuitry of the SNS are all contained within a Nb tube of aspect ratio $R\approx4$ for flux shielding. No external cables enter this shielded region to minimize external noise picked up by our detector. This ensures that the flux noise floor of this apparatus sits at the minimum level of $\Phi<4\mu\Phi_0\ \mathrm{Hz}^{-1/2}$ quoted by the manufacturer for the entire temperature range of the study, as shown in Extended Data Fig. 1.

Operation. A typical operation cycle consists of cooling down to 1.2 K and then setting the operating temperature in the range from 1.2 K to above 4 K, with temperature stability at each step of 2.5 mK. Once the temperature is stable at a desired set-point, we record the flux noise $\Phi(t)$ generated by our sample and then evaluate its spectral density using a spectrum analyser. Unprocessed data at each temperature consist of five datasets with a bandwidth of 2.5 kHz, each of which is the outcome of averaging 1,000 acquisitions with acquisition time of (resolution bandwidth)$^{-1}$, providing the output as voltage noise spectral density detected at the SQUID, $S_V(\omega, T)$.

Calibration. The transfer function C between the pickup coil and the SQUID is calibrated by driving a small known flux $\Phi_{\text{test}}(\Phi_0)$ via a drive coil (inserted into the pickup coil) through the pickup coil and recording the corresponding SQUID output voltage V_{S}. In this case (Extended Data Fig. 1)

$$C = \frac{V_{\text{S}}}{0.684} \frac{1}{\Phi_{\text{test}}(\Phi_0)} \tag{17}$$

We find that $C = 0.015$. The spectral density of the magnetic-flux noise within the sample is obtained as

$$S_{\Phi}(\omega, T) = \frac{S_V(\omega, T)}{C^2} \tag{18}$$

To relate $S_{\Phi}(\omega, T)$ to the magnetic-field noise spectral density generated within our sample, $S_{B_z}(\omega, T)$, we consider the cross-sectional area of the sample $\sigma = 1.4 \times 10^{-6} \pm 17\%$, yielding

$$S_{B_z}(\omega, T) = \frac{S_{\Phi}(\omega, T)}{\sigma^2} \tag{19}$$

in units of T^2 s.

Flux noise signal strength. A comparison between a typical magnetic-flux noise spectral density distribution from a sample and the noise spectral density from an empty pickup coil is shown in Extended Data Fig. 2 for a bandwidth of 1 Hz to 2.5 kHz. The plateau of the flux noise spectral density from $Dy_2Ti_2O_7$ is higher than the noise floor level by a factor of 1.5×10^6. Mechanical noise peaks in the empty coil flux signal and the $Dy_2Ti_2O_7$ flux signal have been deleted manually. We note that the plateau for the flux noise spectral density signal of monopoles from $Dy_2Ti_2O_7$ goes down to at least 1 Hz.

Sample geometry effects. Shape effects could occur in such spin noise measurements. This is because even though we measure a cuboidal sample with a coil around its middle, the spins at the ends of the sample still contribute partially. Our experiments measure flux through the pickup coil due to dipole fields generated by the spins in the sample, and the noise comes mainly from spin flips (that is, magnetic monopole hops). The detectable flux caused by a single spin in the sample depends on the location and direction of that spin. Some spins are 'invisible' (for example, spins pointing to a direction in the x–y plane) and some have a greater effect, for example, spins near the plane of the coil that are pointing along z. If there is a fluctuation of the magnetic moment of the whole sample that results in a net moment, it will produce a net demagnetization field experienced by all of the spins (potentially affecting their dynamics) that is shape-dependent.

Data analysis. *Fitting.* The flux noise spectral density floor measured for an empty pickup coil in the SNS (that is, the background noise S_{Φ}^{bcg}) is fitted to a smooth polynomial function S_{Φ}^{f}. Because the noise floor does not vary with temperature, the same function S_{Φ}^{f} is then subtracted from the measured $Dy_2Ti_2O_7$ noise, $S_{\Phi}^{\text{DTO}}(\omega, T)$ for all temperatures, to obtain the reported noise spectral density $S_{\Phi}(\omega, T)$ dataset shown in Fig. 3.

These post-processed data are then fitted with the empirical equation (6) using the least-squares method for a bandwidth of 16 Hz–2.5 kHz for all temperatures. Although the plateau in the flux noise spectral density $S_{\Phi}(\omega, T)$ goes down to at least 1 Hz for all temperatures, to optimize the data acquisition times to about 1 h per temperature, for all spectra shown in Fig. 3 the lower limit for the bandwidth of the data used in regression analysis is set at 16 Hz. The time constant, $\tau(T)$, the power-law exponent for the frequency, $b(T)$, and $S_{\Phi}(0, T)$ are free parameters in the fitting procedure, and fits for all temperatures are of high quality, with $R^2 > 0.99$. The residuals of these fits are shown in Extended Data Fig. 3. We established that the flux noise spectral density from $Dy_2Ti_2O_7$ is consistent for different single crystals of the material, as shown in Extended Data Fig. 4.

Comparison of time constants. It has been established empirically that the susceptibility-derived time constants $\tau_{\text{M}}(T)$ representing the magnetization dynamics of $Dy_2Ti_2O_7$ diverge with decreasing T[22–24] and are probably heterogeneous[25,35]. This type of a.c. susceptibility measurement has been made for $Dy_2Ti_2O_7$ in different sample shapes ranging from polycrystalline samples[24] to toroidal single crystals[25,35]. Yaraskavitch et al. established that the time constants $\tau_{\text{M}}(T)$ measured from SQUID-based susceptibility measurements of rod-shaped samples were in good qualitative agreement with $\tau_{\text{M}}(T)$ values reported in both Snyder et al.[22] and Matsuhira et al.[23] Eyvazov et al.[35] verified quantitative agreement between $\tau_{\text{M}}(T)$ from a.c. susceptibility measurements and $\tau_{\text{M}}(T)$ from Yaraskavitch et al.[24].

In Extended Data Fig. 5, we show the GR time constants $\tau(T)$ obtained from our flux noise experiments. These clearly follow a quantitatively equivalent trajectory to the a.c. susceptibility $\tau_{\text{M}}(T)$ of refs [25,35] and thus correspond well with the $\tau_{\text{M}}(T)$ values derived from numerous susceptibility studies of this material[22–25]. However, the correspondence between $\tau_{\text{M}}(T)$ and $\tau(T)$ reported in this work remains to be understood within a quantitative microscopic theory.

Additionally, evidence for a heterogeneous distribution of microscopic spin relaxation rates contributing to $\tau_{\text{M}}(T)$ has been adduced from the stretched-exponential form of the time dependence of magnetization[25,35] in $Dy_2Ti_2O_7$. Considering the related a.c. susceptibility studies[22–25,35] and the similarity between $\tau_{\text{M}}(T)$ and $\tau(T)$, we estimate that any effects of such heterogeneity on the flux noise spectrum $S_{\Phi}(\omega, T)$ would first become visible at temperatures below $T = 1$ K. Therefore, they are unlikely to have been detected in these first SNS studies.

Variance in magnetic-flux noise. We note that the measured variance of the signal $\Phi(t)$, σ_{Φ}^2, is approximately constant as a function of temperature, as shown in Extended Data Fig. 6. This variance is determined at each temperature by integrating the measured flux noise spectrum over the frequency.

$$\sigma_{\Phi}^2 = \int_0^{\infty} S_{\Phi}(\omega) \mathrm{d}\omega \tag{20}$$

The result in Extended Data Fig. 6 may appear surprising because one would generally expect that the fluctuations would be rapidly suppressed with falling temperatures. However, although the number of magnetic monopoles in $Dy_2Ti_2O_7$ is believed to decrease rapidly (exponentially in the simplest theory) with falling temperature, the integrated magnetic-flux noise power in the temperature range of our studies remains approximately constant. As explained in Methods section 'Statistics of monopole number fluctuations', this phenomenology is empirically consistent with the measured $\tau(T)$. However, it will require further theoretical and experimental studies to determine and understand its evolution towards lower temperatures.

Calibration of Monte Carlo time step. *Inter-calibration of timescales.* To obtain a correspondence between MC time step and actual time, we assume that the MC temperature is equal to the measured temperature of the experiment in the range 1.2 K–3 K. We then compare the GR time constants obtained from fitting $S(\omega, T)$ to $\tau(T)/\{1+[\omega\tau(T)]^b\}$ for: (a) the MC DSI model simulations in Fig. 2b to yield $\tau_{\text{MC DSIM}}(T)$ and (b) the experimental data in in Fig. 3a to yield $\tau_{\text{experiment}}(T)$. The temperature T is used as the implicit variable. The slope of a linear fit of $\tau_{\text{MC DSIM}}(T)$ versus $\tau_{\text{experiment}}(T)$ yields the correspondence between MC step and actual time. The result yields that in these simulations 1 MC step $= 83 \pm 11$ µs, which is then used throughout our study. The possibility of nonlinearity in the correspondence of our MC step to seconds, as reported in other MC simulations[36], will require future studies on how scaling the periodic boundary conditions and MC sample volumes affects the linear correspondence that is typically used in similar experiment–MC comparisons[10].

Data availability

The data that support the findings of this study are available from the corresponding author upon reasonable request.

34. Metropolis, N., Rosenbluth, A. W., Rosenbluth, M. N. & Teller, A. H. Equation of state calculations by fast computing machines. *J. Chem. Phys.* **21**, 1087–1092 (1953).
35. Eyvazov, A. B. et al. Common glass-forming spin liquid state in the pyrochlore magnets $Dy_2Ti_2O_7$ and $Ho_2Ti_2O_7$. *Phys. Rev. B* **98**, 214430 (2018).
36. Takatsu, H. et al. AC susceptibility of the dipolar spin ice $Dy_2Ti_2O_7$: experiments and Monte Carlo simulations. *J. Phys. Soc. Jpn* **82**, 104710 (2013).

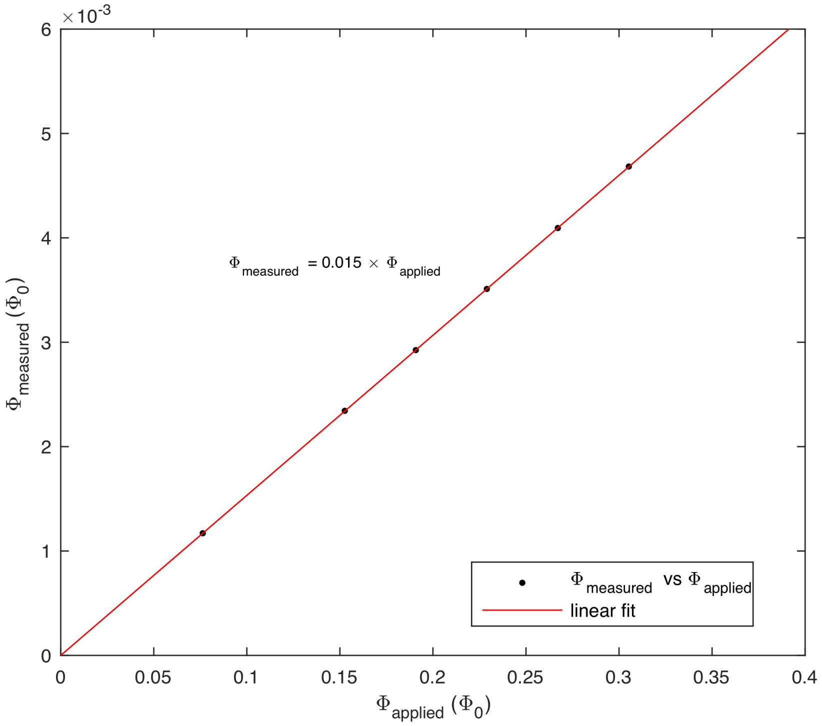

Extended Data Fig. 1 | Sensitivity calibration of magnetic-flux noise spectrometer. Here we show the linear relationship between a flux applied to the pickup coil via a drive coil (Φ_{applied}) and flux output by the SQUID (Φ_{measured}). The slope gives the transfer function between the pickup coil and the SQUID.

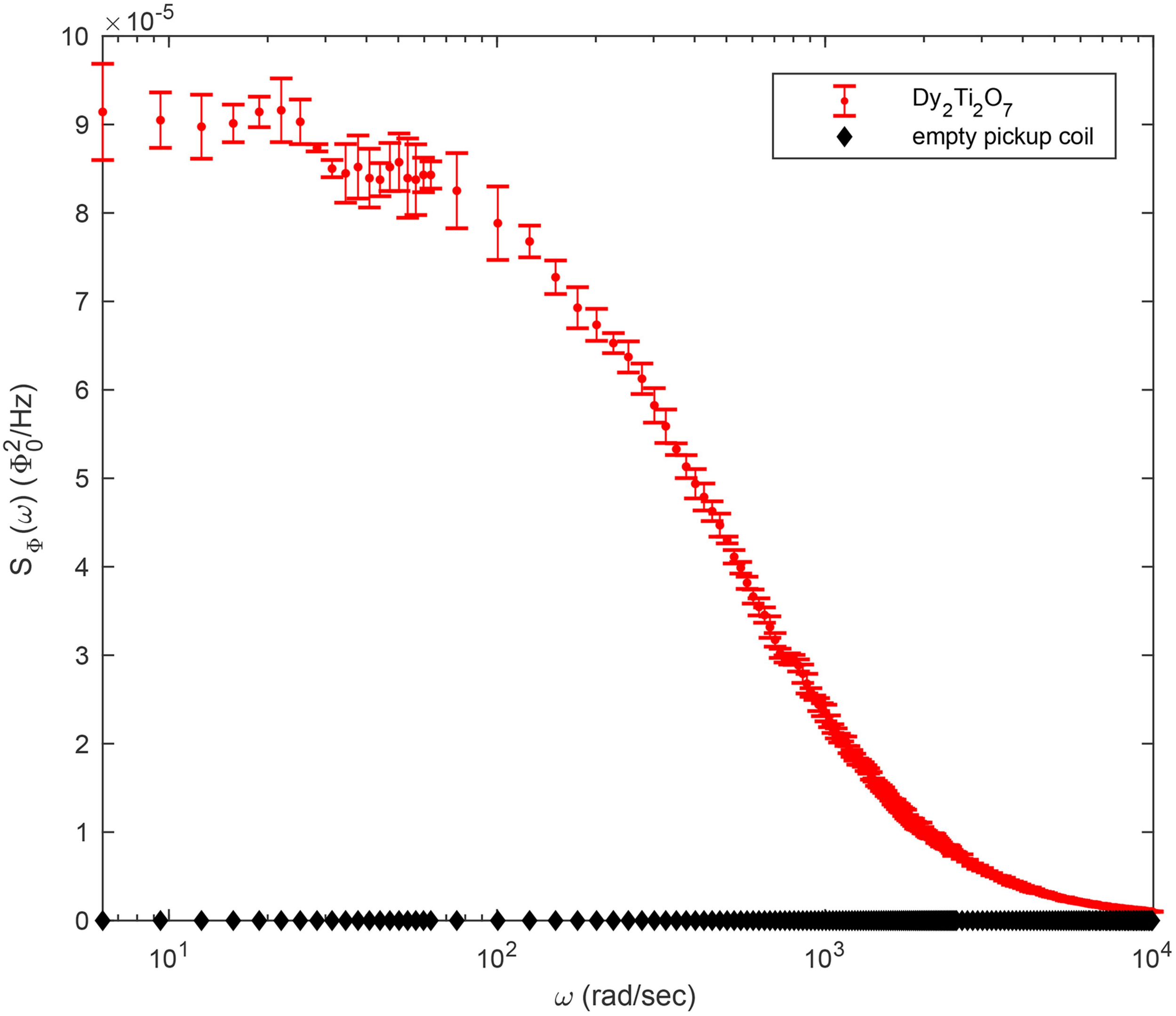

Extended Data Fig. 2 | Comparison of $Dy_2Ti_2O_7$ magnetic-flux noise with background noise. Typical spectrum of magnetic-flux noise spectral density from a $Dy_2Ti_2O_7$ sample (at 1.22 K) compared with that of an empty pickup coil corresponding to ~$16.8 \times 10^{-12}\Phi_0^2$ Hz^{-1}. The black data points have been shifted vertically for clarity. Error bars represent the standard deviation of each data point, extracted from an average of five independent $Dy_2Ti_2O_7$ flux noise datasets.

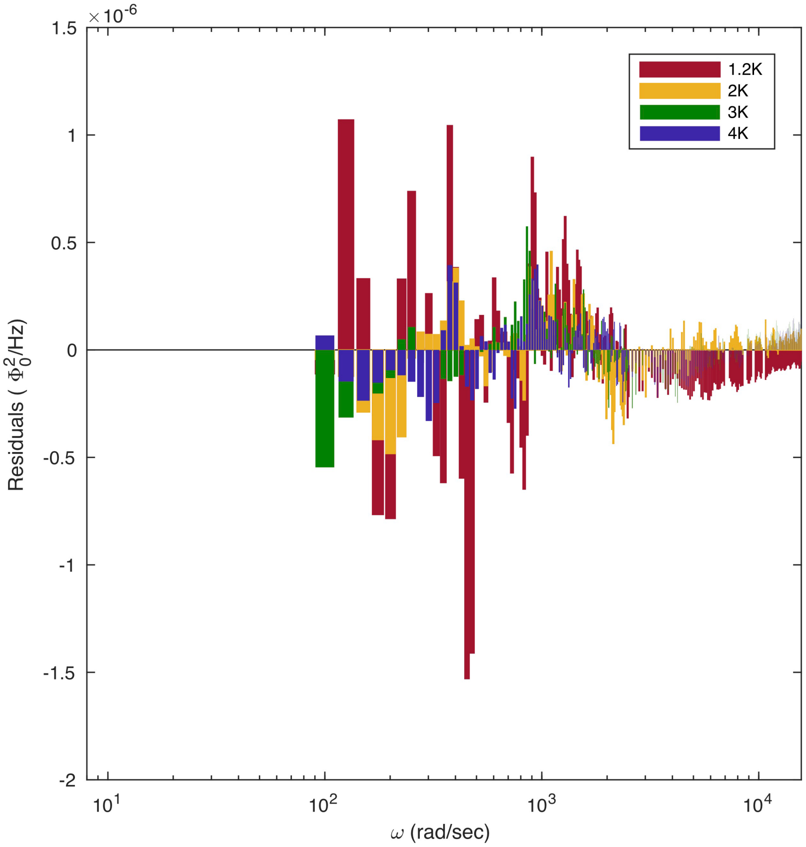

Extended Data Fig. 3 | Quality of fits to measured flux noise spectral density. Residuals ($S_{\Phi}(\omega, T) - S_{\mathrm{fit}}(\omega, T)$) for fits of the measured flux noise spectral density (Fig. 3) with equation (5) are shown for four temperatures.

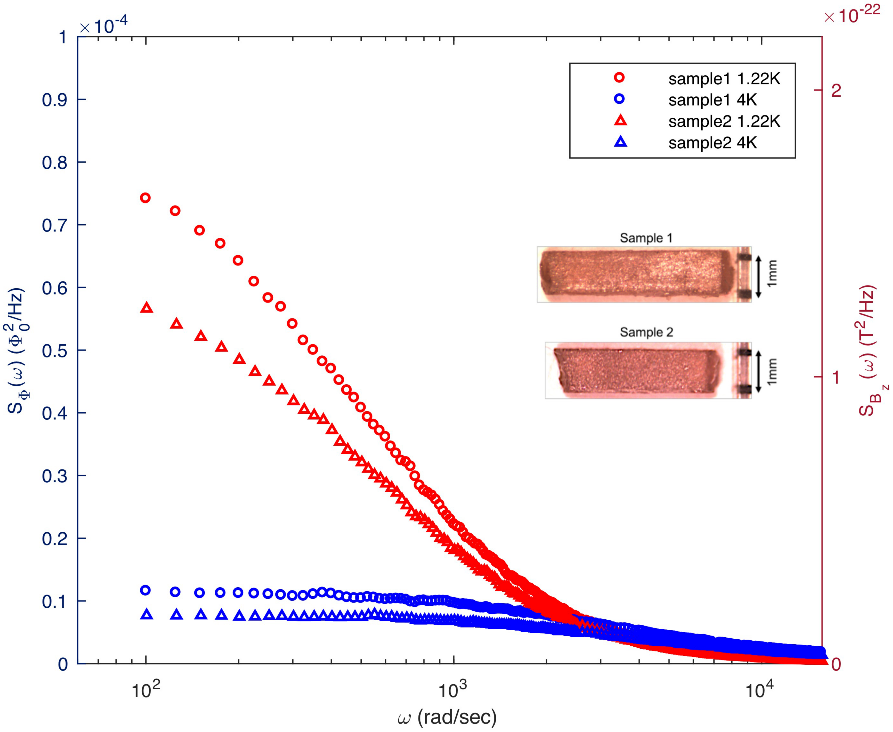

Extended Data Fig. 4 | Comparison of magnetic-flux noise from different $Dy_2Ti_2O_7$ samples. Plot of magnetic-flux noise $S_\Phi(\omega, T)$ from two different rod-shaped $Dy_2Ti_2O_7$ samples. We observe that the $S_\Phi(\omega, T)$ distributions are very similar and therefore this experiment is qualitatively repeatable for single crystals of $Dy_2Ti_2O_7$. The differences in magnitude and time constant are due to the geometrical differences between the two samples.

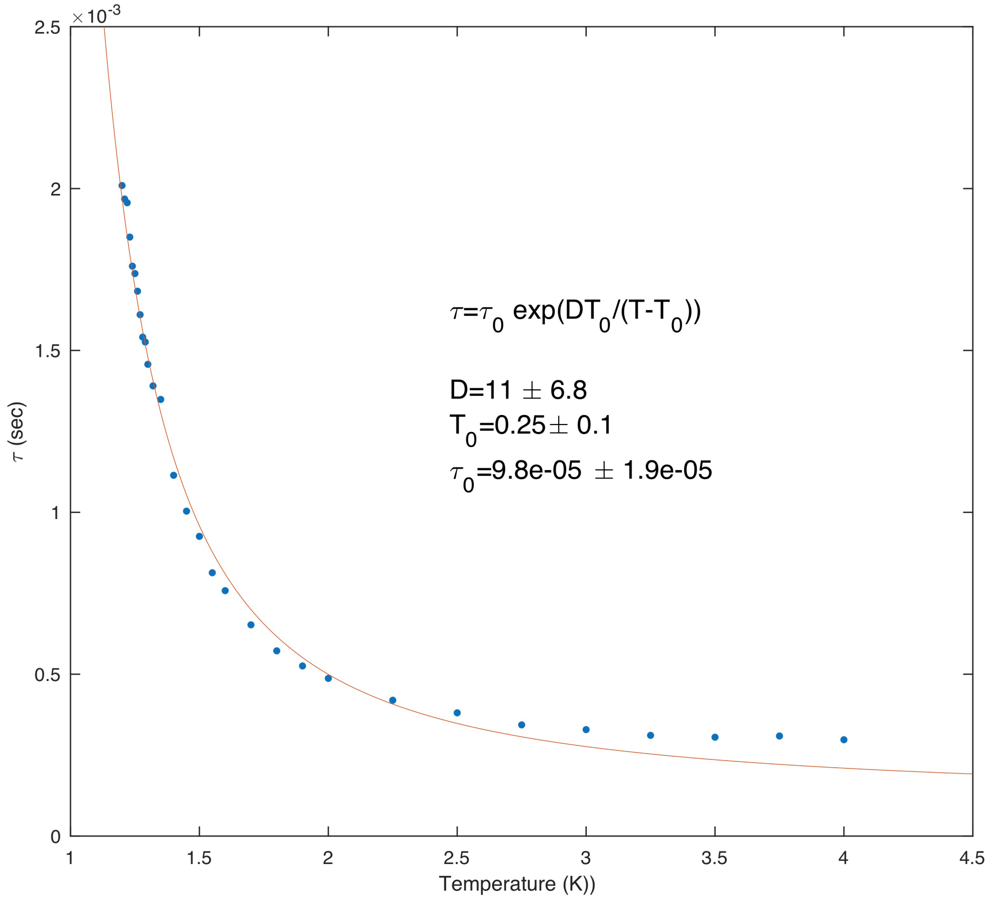

Extended Data Fig. 5 | Magnetization relaxation time constants from flux noise spectra. Time constant obtained from fits to the measured $S_{\Phi}(\omega, T)$ data shown in Fig. 3. The time constant $\tau(T)$ derived from the flux noise behaves in a super-Arrhenius fashion, $\tau(T) = \tau_0 \exp[DT_0/(T - T_0)]$, consistent with previous measurements of a.c. susceptibility time constants $\tau_M(T)$ (ref. [35]), which also exhibited super-Arrhenius behaviour with $\tau_0 \approx 1.4 \times 10^{-4}$ s, $D \approx 14$, $T_0 \approx 0.26$ K.

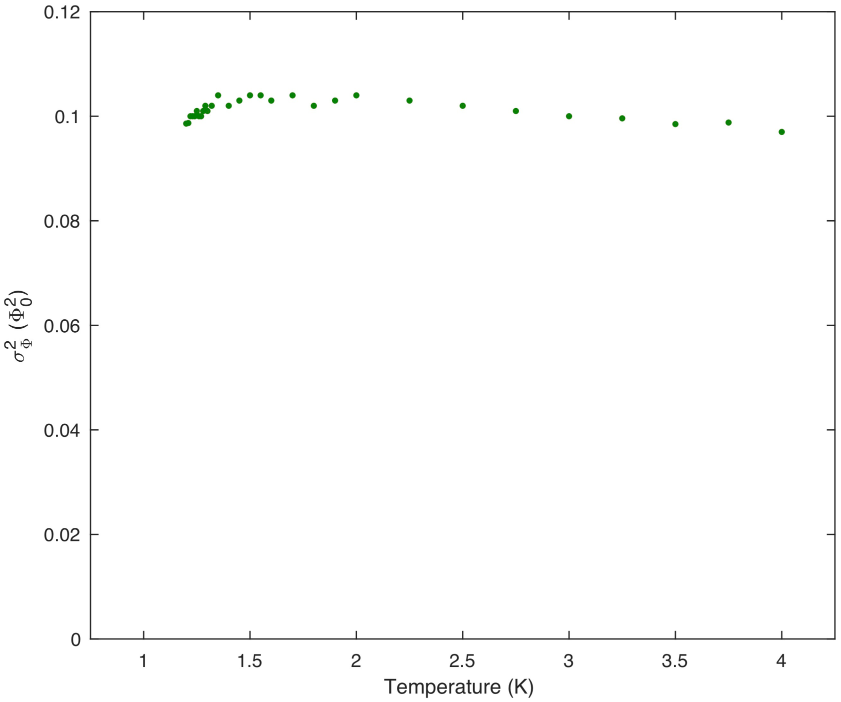

Extended Data Fig. 6 | Variance of $Dy_2Ti_2O_7$ magnetic-flux noise versus temperature. Measured variance of flux σ_Φ^2, showing that it is approximately constant as a function of temperature in the range displayed.